JGR Space Physics

RESEARCH ARTICLE
10.1029/2023JA031598

Electron Aurora and Polar Rain Dependencies on Solar Wind Parameters

S. Bouriat[1,2,3], S. Wing[4], and M. Barthélémy[2,3]

[1]SpaceAble, Paris, France, [2]CNRS, IPAG, University of Grenoble Alpes, Grenoble, France, [3]CSUG, University of Grenoble Alpes, Grenoble, France, [4]Applied Physics Lab, Johns Hopkins University, Baltimore, MD, USA

Key Points:

- We produced 2D maps of the electron precipitation in the auroral oval and polar cap
- Electron flux peaks at midnight to the prenoon sector; consistent with curvature and gradient drifts and very low frequency wave induced pitch angle scattering
- Polar rain increases with |IMF B_z| and the precipitating electron flux in the auroral oval increases as the solar wind velocity enhances

Correspondence to:

S. Bouriat,
simon.bouriat@spaceable.eu

Citation:

Bouriat, S., Wing, S., & Barthélémy, M. (2023). Electron aurora and polar rain dependencies on solar wind parameters. *Journal of Geophysical Research: Space Physics*, *128*, e2023JA031598. https://doi.org/10.1029/2023JA031598

Received 22 APR 2023
Accepted 17 AUG 2023

Abstract Data analysis was performed using 17 years of Defense Meteorological Satellite Program SSJ/4/5 data to characterize the relations between the solar wind parameters and the electron low-energy fluxes measured on both magnetic poles (magnetic latitude above 55°). Inputs are solar wind velocity, density, dynamic pressure, and B_z of the interplanetary magnetic field. The median of electron energy flux for each MLAT-MLT pair has been computed for given values of solar wind condition parameters. Results highlight that high velocity, density or pressure implies higher energy flux overall, higher polar rain energy fluxes, and wider nightside oval. There seems to be a positive correlation between polar rain and solar wind density, contrary to a previous study. As a function of B_z, the oval width has a "U" shape and the polar cap activity a "V" shape, with their minimum at B_z around zero.

Plain Language Summary Auroral precipitations are indicators of the magnetosphere-ionosphere coupling. Here, data analysis was performed using 17 years of Defense Meteorological Satellite Program SSJ/4/5 data to characterize the relations between the solar wind condition parameters and the electron low-energy fluxes measured on both magnetic poles (magnetic latitude above 55°). Inputs are solar wind velocity, density, dynamic pressure, and B_z of the interplanetary magnetic field, from NASA's OMNIWeb database. Median of electron energy flux for each MLAT-MLT pair has been computed for given values of solar wind parameters. Results highlight that high velocity, density or pressure implies higher energy flux overall, higher polar rain energy fluxes, and wider nightside oval. There seems to be a positive correlation between polar rain and solar wind density, contrary to a previous study. As a function of B_z, the oval width has a "U" shape and the polar cap activity a "V" shape, with their minimum at B_z around zero. This work is a unique contribution to the field as it put together a global picture of the electron precipitation that scientific community can use as a reference for how the oval and polar rain vary at different magnetic local time (MLTs) values as a function of solar wind parameters.

1. Introduction

The aurora, also known as the northern lights, has fascinated people since ancient times. The area above the Earth's poles where auroras are visible is commonly referred to as the auroral zone. However, it was not until the early 1960s that scientists realized that this region has a distinct shape resembling a ring or an oval. As a result, it was given the name auroral oval (Feldstein, 2016, see review).

The aurora light emission is primarily caused by ions and electrons. These particles originate from the solar wind and the magnetosphere and interact with the neutral components of the upper atmosphere, causing them to ionize and excite. The majority of the precipitating particles on the dayside oval, including the cusp, mantle, low-latitude boundary layer (LLBL), open-field line LLBL (open-LLBL), and high-latitude boundary layer regions, come from the solar wind (Fujimoto et al., 1998; Lockwood et al., 1993; Lyons et al., 1994; Newell & Meng, 1992; Shi et al., 2013, 2009; Wing et al., 1996, 2001), while those at the equatorward portion of the oval such as boundary plasma sheet (BPS) and central plasma sheet (CPS) come from the magnetosphere (Newell & Meng, 1992; Newell et al., 2004). On the nightside oval, the majority of precipitating particles are magnetospheric in origin (Newell et al., 2004, 1991). The dayside and nightside particle precipitation regions have different characteristics, but there are similarities and connections between the two regions. For example, the particles in the BPS and CPS are the nightside plasma sheet particles that have curvature and gradient-drifted to the dayside and then precipitate (Newell & Meng, 1992; Wing et al., 2023). However, it should be noted that these magnetospheric particles whether on the dayside or nightside, originate from solar

wind plasma that has entered the magnetosphere several hours to over 15 hr earlier, depending on the location within the magnetosphere and the prevailing solar wind conditions (Berchem et al., 2014, 2016; Borovsky et al., 1998; Sorathia et al., 2019; Wing et al., 2014, 2006, 2005; Wing & Newell, 1998). Hence, the particle precipitation in the polar region, whether on open or closed field lines, should have dependencies on the solar wind properties.

The position, structure, intensity, and latitudinal width of the auroral oval can vary significantly due to fluctuations in the solar wind. Previous studies investigating the drivers of auroral oval variability have primarily focused on the micro or mesoscale structures within the auroral oval, typically limited to a few magnetic local time (MLT) (Gabrielse et al., 2021; Johnson et al., 2021; Sergeev et al., 2004; Zhu et al., 2018). Fewer studies examined the global scale of electron precipitation within the entire auroral oval or polar region across all MLTs. For example, Wing et al. (2013) studied the evolution of the electron aurora oval as a function of the substorm phase at the global scale. Likewise, Newell, Sotirelis, and Wing (2009) studied the dependencies of the electron aurora on the strength of solar wind driving, as determined by solar wind-magnetosphere coupling functions, and seasonal variations at a global scale. Seasonal dependence of global-scale auroral particle precipitation has been studied both with models (Wiltberger et al., 2009) and with observations from the Defense Meteorological Satellite Program (DMSP) satellites (Newell et al., 2010). Finally, Liou et al. (2007) presented a case study of the auroral oval response to a long duration of high solar wind dynamic pressure.

The precipitating electrons are the field-aligned plasma sheet electrons that are in the loss cone and precipitate in the ionosphere. Most of these electrons would not mirror back to the magnetosphere. However, in the magnetosphere, the electrons in the loss cone can be replenished by pitch angle scattering of the non-field aligned electrons through wave-electron interactions. Energy exchange between electrons and waves can occur when the wave frequency and the frequency of the electron periodic motion match, resulting in violation of adiabatic invariant and diffusion in phase space, which can effectively alter the electrons' pitch angles. Very low frequency (VLF) whistler-mode chorus waves have been proposed as a leading mechanism for pitch angle scattering of the plasma sheet electrons (Ni et al., 2016; Summers et al., 1998). Thorne (2010) showed that the VLF whistler-mode chorus waves are particularly active from midnight to noon (see their Figure 1). The local time distribution of these waves and their intensities should have an impact on the local time distribution and intensity of the precipitating electrons, particularly diffuse electrons.

The present study investigates statistically the global scale of the position, structure, intensity, and latitudinal width of the precipitating electrons within the entire auroral oval and polar cap due to solar wind velocity, density, dynamic pressure, and the B_z component of the interplanetary magnetic field (IMF).

2. Data and Methodology

2.1. DMSP Satellites and Data

The DMSP satellites are in Sun-synchronous nearly circular polar orbits at about 845 km altitude, with orbital inclinations of 98.7°. The areas with the least amount of coverage occur around post-noon and post-midnight local time, with the exception of regions at high magnetic latitudes where the coverage is more uniform. A significant number of measurements obtained from DMSP are concentrated within the intervals of 5–10 MLT and 16–21 MLT (as seen in Figures A5–A8).

The SSJ/4 and SSJ/5 instruments (Special Sensor Precipitating Electron and Ion Spectrometer [SESS]) are respectively part of the Space Environment Monitor and SESS packages. They measure the flux of precipitating electrons and ions through a curved plate electrostatic analyzer for electrons protons and alpha-particles in the energy range 0.03–30 keV, with one complete spectrum each obtained per second (Hardy et al., 1984). The SSJ/4 instrument was deployed on spacecraft belonging to the DMSP series, specifically from F6 to F15, while the SSJ/5 instrument was deployed on satellites F16–F19. The satellites are three-axis stabilized, and the detector apertures always point toward local zenith. At the latitudes of interest in this paper, this means that only highly field-aligned particles well within the atmospheric loss cone are observed.

Data from the SSJ/4 and SSJ/5 were used to highlight changes in polar auroras. The satellites (and corresponding years and instrument) were available on the Coordinated Data Analysis Web (CDAWeb) interface of the Goddard Space Flight Center, spanning 17 different years as shown in Table 1. The data collected include the

Table 1
This Table Shows the Available Data Years for Each Defense Meteorological Satellite Program Satellite

	1987	1988	...	2000	2001	2002	2003	2004	2005	2006	2007	2008	2009	2010	2011	2012	2013	2014
SSJ4																		
F06	■																	
F07	■																	
F08	■																	
F09		■																
F12				■	■	■												
F13				■	■	■	■	■	■	■	■							
F14				■	■	■	■	■	■									
F15				■	■		■	■	■	■	■	■	■					
SSJ5																		
F16														■	■	■	■	■
F17													■	■	■	■	■	■
F18														■	■	■	■	■

Note. Green cells indicate data availability.

1 s resolution total electron energy flux (in eV/cm^2/ster/s), which is obtained by integrating the differential energy fluxes measured by DMSP across the energy range. Data are displayed in AACGM coordinates (Baker & Wing, 1989).

As pointed out by Newell, Sotirelis, and Wing (2009), the operational lifespan of several detectors has led to degradation of sensitivity and consequently, decreased reliability in boundary identification in recent years. Furthermore, the low-energy ion head of certain SSJ/4 detectors has been launched in a sub-optimal condition, thereby diminishing the quality of ion precipitation data.

2.2. Solar Wind Data

The solar wind data gathered on NASA's OMNIWeb database are not in situ measurements. They consist of high-resolution (1 min) solar wind and IMF data at the Earth's magnetopause: data from ACE, WIND, IMP 8, and Geotail spacecraft that have been processed and time-shifted to the Bow Shock Nose (BSN) (King & Papitashvili, 2006). The solar wind and IMF data used in this paper are only the IMF B_z in GSM coordinates (in nT), the solar wind proton density (in cm^{-3}), velocity, (in km·s^{-1}), and ram pressure (in nPa and derived from particles' densities, speeds, and masses $\propto nv^2$).

In this study, we combined the data from both the north and south hemispheres, as we considered it more appropriate for our research objectives. Therefore, we removed the *X*- and *Y*-components of the magnetic field, assuming that their effects are symmetric in both hemispheres and will cancel each other out.

2.3. Methodology

As previously mentioned, we combined data from the North and South poles (above and below 45° and −45° MLAT, respectively) and averaged it instead of subsampling to maintain a 1 min resolution. We obtained 1 min resolution solar wind, magnetic field, and plasma data from the OMNI interface at Earth's BSN and applied a 30 min wide moving average. Specifically, we replaced each data point at time T_0 with the mean value of all data points in the time window $[T_0 - 29 : T_0]$. We required a minimum of 10 points in the window for us to accept the average and discard other data points.

We binned the four solar parameters (solar wind flow speed, density, temperature, and dynamic pressure) into eight bins each, with each bin having specified limits. Here are the limits for each parameter:

- **IMF B_z in GSM** coordinates: [−∞, −9, −6, −3, 0, 3, 6, 9, +∞] nT.
- Solar wind pressure: [0, 1, 2, 3, 4, 5, 8, 15, +∞] nPa.
- Solar wind proton density: [0, 2, 4, 6, 8, 10, 15, 20, +∞] cm^{-3}.
- Solar wind flow speed: [0, 300, 400, 500, 600, 700, 800, 900, +∞] km·s^{-1}.

In these limits, the right endpoint is not included. For example, the first bin for solar wind flow speed is from 0 to 300 km·s^{-1}, including all values between 0 and 300 km·s^{-1}, but not including 300 km·s^{-1}.

Finally, we grouped DMSP data falling into a given bin (e.g., all DMSP measurements for B_z between −9 and −6 nT). Then, we computed the median of these DMSP data for all given MLAT-MLT pairs. We plotted the resulting medians in a polar plot, where each compartment represents a 1°(MLAT) × 1 hr(MLT) area and shows the corresponding median value of DMSP measurements using a base-10 a logarithm for clarity. Essentially, we generated a polar plot of DMSP measurements for each instance where the average of a solar wind driver in the past 30 min fell within a particular range (e.g., when the average of B_z in the past 30 min was between −9 and −6 nT—see Figure 4b).

The outcome was one graph per solar wind parameter per bin, with each compartment on the polar graphs measuring 1°(MLAT) × 1 hr(MLT) and displaying the corresponding median value of DMSP measurements. To improve clarity, the graphs shown in Figures 1–4 display only MLAT values above 55°.

Throughout the following descriptions, when we refer to the electron energy flux, we are referring to the base-10 logarithm of the total electron energy flux, which represents the amount of energy carried by the electrons and is measured in eV/cm^2/ster/s.

3. Results

3.1. Dependence of Electron Energy Flux on Solar Wind Speed

Figure 1 shows the base-10 logarithm of the total electron energy flux within the entire auroral oval as a function of solar wind speed. Several things are worth noting. First, the electron energy flux is higher around midnight to noon than from noon to midnight. This can be explained by the electron gradient and curvature drifts and the VLF whistler-mode chorus waves. Electrons coming earthwards following reconnections in the magnetotail would also curvature and gradient drift eastward toward dawn. Electrons that are field-aligned (pitch angle 0°) are quickly lost through precipitation, but the field-aligned electrons are replenished by pitch angle scattering. The leading mechanism for pitch angle scattering is the electron interactions with the VLF whistler-mode chorus waves, which have been shown to be active at midnight-noon local time (Ni et al., 2016; Reeves et al., 2009; Summers et al., 1998; Thorne, 2010). Once we enter the post-noon region, the whistler-mode chorus wave's activity is reduced and we see less pitch angle scattering, and hence a reduction in electron energy flux. The MLT profile and the dawn-dusk asymmetry seen in Figure 1 are similar to those of the diffuse electron precipitation in Wing et al. (2013), which is not surprising because most of the electrons are diffuse electrons.

As the solar wind speed increases, the electron energy flux also increases, from the smallest velocities to the largest velocities. This relationship can be attributed to the increased occurrence of substorms and subsequent wave activities, which would increase with higher solar wind speeds (Newell et al., 2016). Substorm injections would energize and transport particles from the plasma sheet inward, resulting in ion temperature anisotropy and the growth of VLF whistler-mode chorus waves. These waves, in turn, can enhance electron pitch angle scattering. Additionally, Figure 1 shows that the auroral oval extends equatorward to smaller latitudes as the solar wind velocity increases.

Understanding the increase in the width of the auroral oval is more challenging since it is not consistent across different MLT regions. By setting the boundary of the oval to 10 eV/cm^2/ster/s, we can see that the approximate width of the auroral oval generally increases with as the solar wind velocity enhances, except for the 11–16 MLT region, where it appears to remain roughly the same and increase only in the last two panels. Note that whenever we mention MLT regions in the format *X*-*X*', we include the *X*' bin (meaning including the zone between line *X*' and *X*' + 1). Figure A1c in appendix confirms several trends: the oval width in 20–7 MLT region mostly displays a linear increase as the solar wind velocity enhances, the 17–19 MLT region somehow shows an exponential increase, and the 8–10 MLT region exhibits a rapid increase in the oval width from panel A to panel C, followed by a slower increase from panel C to panel F. Finally, computing the oval width over all MLT regions except for region 1 MLT (due to missing values), we observe an increase from an average width of 6.4 MLAT for a median speed of 288 km/s (panel A) to 11.7 MLAT for a median speed of 733 km/s (panel F), corresponding to an 83% increase.

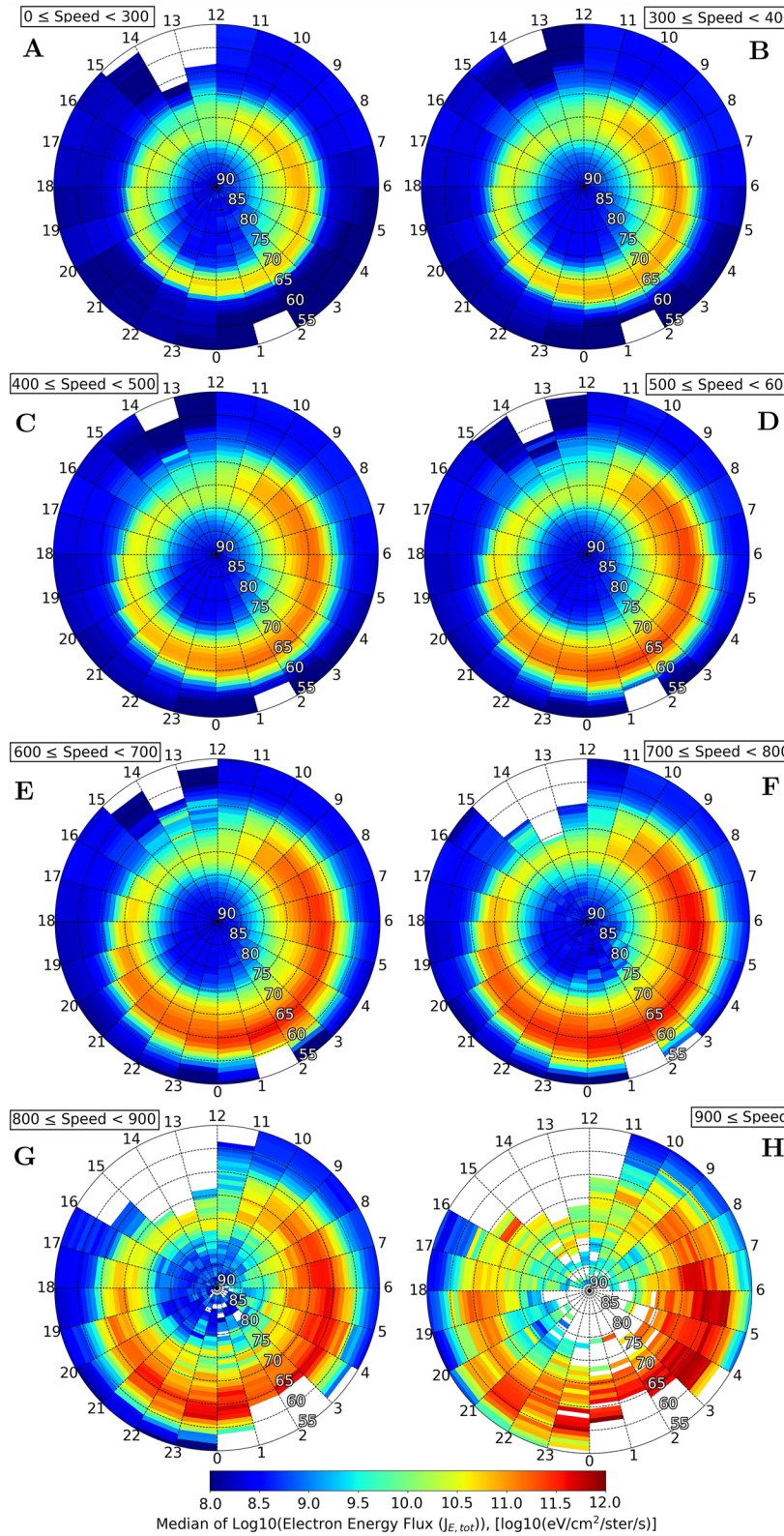

Figure 1. Median of Log_{10} ($J_{E,\mathrm{tot}}$) [eV/cm^2/ster/s] for solar wind speed respectively between 0 and 300 km·s^{-1} (a), 300 and 400 km·s^{-1} (b), 400 and 500 km·s^{-1} (c), 500 and 600 km·s^{-1} (d), 600 and 700 km·s^{-1} (e), 700 and 800 km·s^{-1} (f), 800 and 900 km·s^{-1} (g), 900 km·s^{-1} and infinity (h).

The configuration of the magnetic field lines within the polar cap (poleward of the auroral oval) is believed to be open, that is, connected to the solar wind. Also we set the boundary of the oval to 10 eV/cm^2/ster/s, the polar cap is the region of MLAT above the poleward boundary of the oval, extending from this limit to 90 MLAT. The electron precipitation in the polar cap, which is known as polar rain, originates from the suprathermal (strahl) component of the solar wind electrons (Fairfield & Scudder, 1985). Figure 1 and Figure A1b show that the polar rain electron flux appears to increase with the solar wind velocity, but this effect is not strong. However, we have taken great care to ensure the reliability of the data by retaining only the bins with a minimum of 10 data points. Additionally, we have computed the median of these data points to mitigate any influence from individual anomalous events.

In the polar cap, few solar wind ions can enter the magnetosphere and hence a parallel electric field or potential arises to prevent most solar wind core electrons from entering in order to maintain charge quasi-neutrality (Fairfield et al., 2008; Wing et al., 2015, 1996). However, the solar wind suprathermal electrons (strahl), having higher temperature/energy, can overcome the parallel electric potential and enter the magnetosphere. Borovsky (2021) showed that solar wind velocity is correlated with solar wind strahl. This correlation is consistent with the increase of polar cap electron precipitation (polar rain) energy flux with solar wind velocity seen in Figure 1, although the trend is not strong.

3.2. Dependence of Electron Energy Flux on Solar Wind Density

Figure 2 depicts the relationship between the base-10 logarithm of the electron energy fluxes and the solar wind density. Several observations are evident from Figure 2. First, the same asymmetry observed in Figure 1 is also evident in Figure 2. Specifically, the energy flux is higher at midnight-noon compared to noon-midnight. This can be attributed to the electron curvature and gradient drifts, as well as VLF whistler mode chorus waves, as discussed in Section 3.1.

Second, it appears that an increase in the solar wind density would increase the energy flux in the polar cap, but this effect is weak. When plotting this increase, it seems to behave as a logarithmic function. Figure 2 and Figure A2b show that the mean value of energy flux in the polar cap for panel A is lower than for panel H. When computing it, we see an increase from 8.82 to 9.09 $\log_{10}$(eV/cm^2/ster/s). Borovsky (2021) showed that solar wind density is correlated with solar wind strahl. The increase of polar cap electron precipitation (polar rain) energy flux with solar wind density seen in Figure 2 is consistent with Borovsky (2021) result. Riehl and Hardy (1986) analyzed 262 DMSP passes and found no correlation between polar rain flux and solar wind density. It is not clear why they found no correlation, but their study used a much smaller data set than the present study. One of the explanations given for the Riehl and Hardy (1986) result was that the origin of the polar rain is the solar wind suprathermal electrons, rather than the solar wind core electrons and hence little or no correlation can be expected (Newell, Liou, & Wilson, 2009). However, the positive correlation between solar wind density and strahl intensity found in the more recent study by Borovsky (2021) can help explain why the positive correlation between polar rain electron fluxes and the solar wind density can be expected albeit this effect is rather weak.

However, there is an anomaly. It can be seen that going from panels A (solar wind density 0–2 cm^{-3}) to B (solar wind density 2–4 cm^{-3}), the polar cap energy flux actually decreases slightly from 8.82 to 8.76 eV/cm^2/ster/s on average rather than increases. This seems to be due to the depression in energy flux in the polar cap observed in panel B between 20:00 and 02:00 MLT. It is not clear what causes this anomaly.

Third, as the solar wind density increases, the energy flux in the auroral oval also increases, but the change is not as significant as it is with the velocity. In the case of low density, as in panel A, there is already a high energy flux in the auroral oval. This can be explained by the fact that solar wind density is generally negatively correlated with solar wind velocity, so low solar wind density would correspond to high solar wind velocity (Borovsky, 2020; Maggiolo et al., 2017; Wing et al., 2016, 2022). However, high solar wind density can also result in high solar wind dynamic pressure, which can lead to storms and substorms, thus creating a competing effect that can be observed in this study.

Fourth, as the solar wind density increases, the behavior of the auroral oval width becomes more complex. While Figure 2 provides a visual representation, the full range of variations can be better understood by referring to Figure A2c. Observations show that the 20–7 MLT region experiences a slight decrease in width, followed by an increase. The 8–13 MLT region also shows a small decrease in width. On the other hand, the width in the

14–19 MLT region appears to increase as the solar wind density enhances. Overall, the thickness of the auroral oval seems to transfer from the morning-to-noon region to the evening-to-midnight region, as observed in Figure 2.

3.3. Dependence of Electron Energy Flux on Solar Wind Dynamic Pressure

Figure 3 demonstrates that the electron energy flux increases almost monotonically as the solar wind dynamic pressure enhances. This result is expected as dynamic pressure (or so-called ram pressure) is proportional to nv^2, where n is the solar wind density and v is the solar wind velocity. This pattern for dynamic pressure is consistent with what we have observed for both density and velocity, as shown in Figures A1a and A2a in appendix. In particular, we can see in Figure 3 that the electron energy flux starts at higher values in panel A than in panel A of Figure 1, and does not reach the high values observed in panel H of Figure 1 for high solar wind velocity. Density and velocity anti-correlation can explain this trend.

The effect of dynamic pressure on the width of the auroral oval is also apparent in Figure 3, as we can observe an increase in width and a significant extension of the oval equatorward from panels A to H.

Finally, Figure 3 shows that the polar rain increases as the dynamic pressure enhances. This trend is even clearer than that for solar wind velocity (Figure 1) and solar wind density (Figure 2). This is perhaps unsurprising since the energy fluxes of polar rain increase with n and v, as discussed in Sections 3.1 and 3.2. This increase is further amplified by the dynamic pressure of the solar wind.

3.4. Dependence of Electron Energy Flux on B_z GSM

Figure 4 displays the electron energy flux as a function of the southward component of the IMF B_z. Studies have shown that as the southward B_z increases, the magnetosphere can become more active due to substorms or storms, resulting in particle injections and energization of the particle population in the magnetotail (Kamide et al., 1977; Wing & Johnson, 2009). In Figure 4, a clear dependence can be observed between the north-south component of the IMF and the shapes of both the oval and the polar cap. The polar cap area is delimited by the open-closed field line boundary (OCB), and the B_z component of the IMF is often responsible for magnetic reconnections that impact the OCB's shape (Tulegenov et al., 2023). As demonstrated here, a large southward component of the IMF generally causes the boundary to move equatorward, while a northward component moves the boundary poleward (Tulegenov et al., 2023). Moreover, for positive B_z, a boundary layer can form poleward of the cusp (Shi et al., 2013, 2009), which can shift the poleward edge of the oval to higher latitudes. On the other hand, a large negative B_z corresponds to a lower-latitude average position for the oval (Burch, 1979) and a higher activity in the polar cap. The observations suggest that substorms occurring in isolation or during storms can increase the width and intensity of the oval, as shown in Figure 4, panel A. When the width of the oval is plotted from panels A to H (see Appendix A, Figure A4c), a "U" shape is suggested, with the exception of the 8–16 MLT region, which shows an increasing trend. On average, the width of the oval appears to decrease from panels A to D, with a reduction of the poleward boundary, and then increase again from panels E to H, with an extension of the poleward boundary. From panel A to panel H, the oval evolves from a very asymmetric shape with a thin oval on the dayside and a wide oval on the night side to an approximately symmetric and wide oval centered on the magnetic pole.

The peak value of electron energy flux, which is located between 22:00 and 06:00 MLT in panel A, gradually shifts to the interval between 05:00 and 10:00 MLT as the southward component of the IMF B_z increases from negative to positive values. This phenomenon may be analogous to the effect of solar wind velocity on substorm probability, where high solar wind velocity tends to increase the likelihood of substorms and shifts the peak substorm occurrence toward the nightside. One possible explanation for this behavior is that a strong southward IMF can enhance the generation of whistler mode waves in the magnetosphere, which tend to peak in intensity between 22:00 and 06:00 MLT during substorms. During quieter times, the peak of whistler mode waves may shift to the morning sector, although this cannot be confirmed without direct wave measurements which are not available in our study. The total electron energy flux in the oval exhibits a decreasing trend from panels A to D, corresponding to the shift of the poleward boundary toward lower latitudes. However, it appears that all MLT regions have relatively stable activity levels from panels E to H, on average. These observations are supported

by Figure A4a in appendix, which depicts the median electron energy flux as a function of MLT for various B_z intervals.

The polar cap activity exhibits a distinct V-shape pattern as a function of B_z, as shown in Figure A4b. According to Gussenhoven et al. (1984), the polar rain number and energy fluxes increase as the geomagnetic activity enhances and as IMF B_z reduces when IMF $BB_z < 0$. However, their investigation of IMF B_z only used two bins: IMF $B_z < -2.5$ and 0 nT < IMF $B_z < -2.5$ nT. By using a smaller bin size and more data points, Figure 4 confirms that the polar rain energy fluxes indeed increase when IMF $B_z < 0$ and becomes more negative.

It appears that the polar rain energy flux increases with the |IMF B_z|. For the case of IMF $B_z < 0$, as IMF B_z becomes more negative, the reconnection strength and rate would increase, which would increase the polar rain electron flux (Newell, Liou, & Wilson, 2009), as shown in Figure 4. For the case of IMF $B_z > 0$, it appears that an electron flux also increases with increasing B_z perhaps for the same reason, but there could be other reasons as well. An increase in B_z can reduce the polar cap size (open-closed boundary moves to higher latitude) (Milan et al., 2004; Newell et al., 1997; Tulegenov et al., 2023). Moreover, an increase in IMF B_z can also increase the occurrence of the polar cap arcs, which could be considered an extension of the auroral oval and which have higher fluxes than polar rain (Newell et al., 1997; Troshichev et al., 1988). The effect of the polar cap arcs, whose locations can vary depending on solar wind conditions, would be smeared out in the statistical map shown in Figure 4. All these effects can complicate the determination of the electron flux in the polar cap in Figure 4.

4. Summary and Discussion

In this study, we investigated the global-scale position, structure, intensity, and latitudinal width of the precipitating electrons above 55° MLAT (within both the auroral oval and polar cap) due to solar wind velocity, density, dynamic pressure, and the Z-component of the IMF. Here is a summary of the observations made for each solar wind driver considered.

For solar wind velocity, density, and dynamic pressure, the electron energy flux is always observed to be higher from midnight to noon than from noon to midnight. This phenomenon can be attributed to the electron curvature and gradient drifts, as well as VLF whistler mode chorus waves. This is also true for positive B_z values. However, for negative B_z, this asymmetry seems to appear on either side of the 19:00–07:00 MLTs line.

As a consequence of increasing the solar wind velocity at the BSN:

- The electron energy flux within the auroral oval increases by 83% on average, with the highest flux from midnight to noon. The increase is due to electron gradient and curvature drifts, as well as VLF whistler-mode chorus waves.
- The auroral oval extends equatorward to smaller latitudes as the solar wind velocity increases.
- The polar cap energy flux increases as the solar wind velocity increases, due to an increase in the strahl component of solar wind electrons entering the magnetosphere.
- The approximate width of the auroral oval generally increases as the solar wind velocity enhances, except for the 11–16 MLT region, where it remains roughly the same and increases only in the last two panels.

As a consequence of increasing the solar wind density at the BSN:

- The energy flux in the auroral oval also increases, but the change is not as significant as it is with the velocity. It is higher at midnight-noon compared to noon-midnight, attributed to electron curvature and gradient drifts, as well as VLF whistler mode chorus waves.
- The energy flux in the polar cap increases as the solar wind density enhances, behaving as a logarithmic function. There seems to be a correlation between polar rain and solar wind density, as opposed to what Riehl and Hardy (1986) found, explained by the positive correlation between density and strahl intensity (Borovsky, 2021). However, there is a small decrease when moving from panels A to B, mainly located between 20:00 and 02:00 MLT.

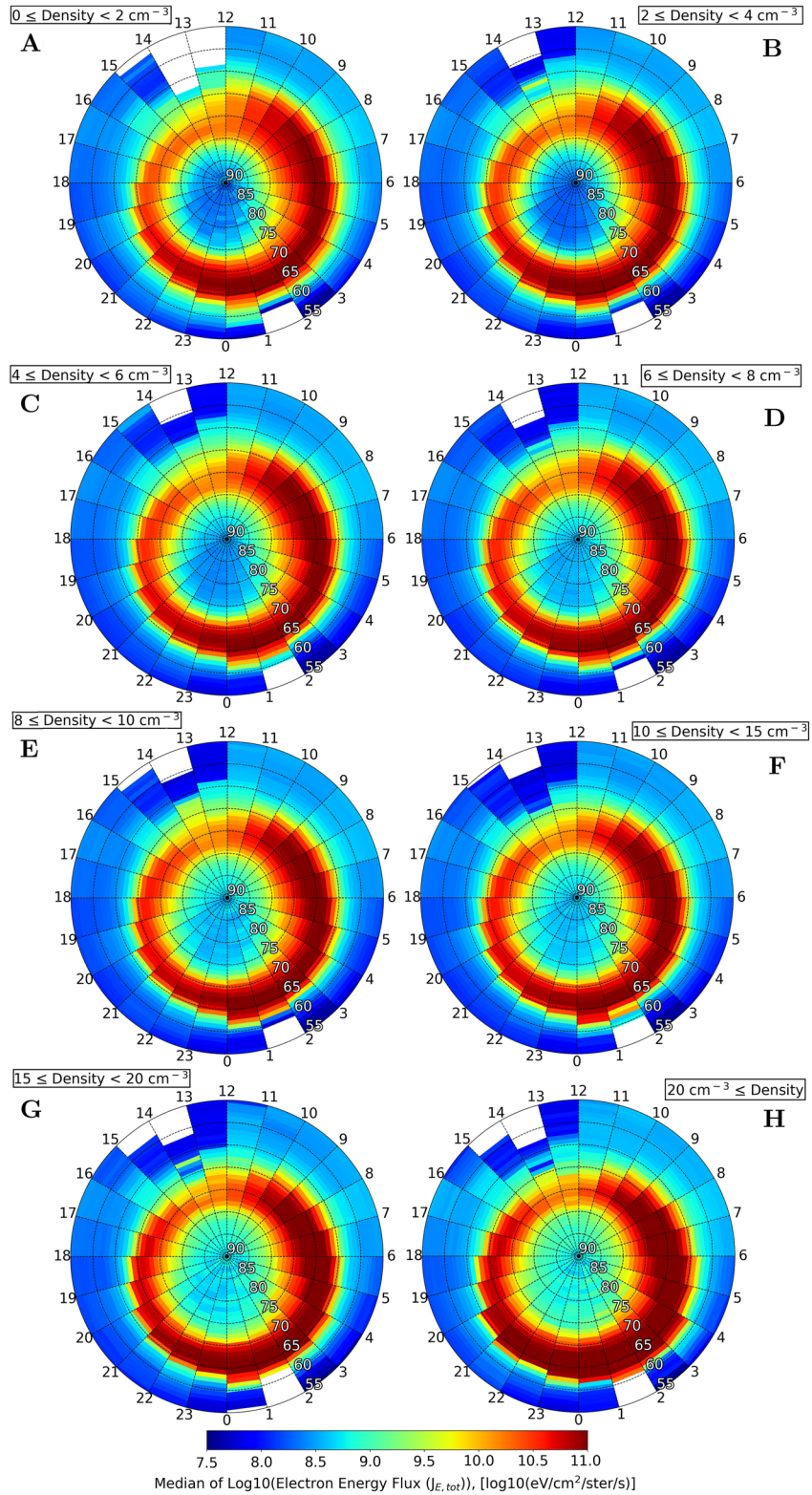

Figure 2. Median of Log_{10} ($J_{E,\mathrm{tot}}$) [eV/cm^2/ster/s] for proton density respectively between 0 and 2 cm^{-3} (a), 2 and 4 cm^{-3} (b), 4 and 6 cm^{-3} (c), 6 and 8 cm^{-3} (d), 8 and 10 cm^{-3} (e), 10 and 15 cm^{-3} (f), 15 and 20 cm^{-3} (g), 20 cm^{-3} and infinity (h).

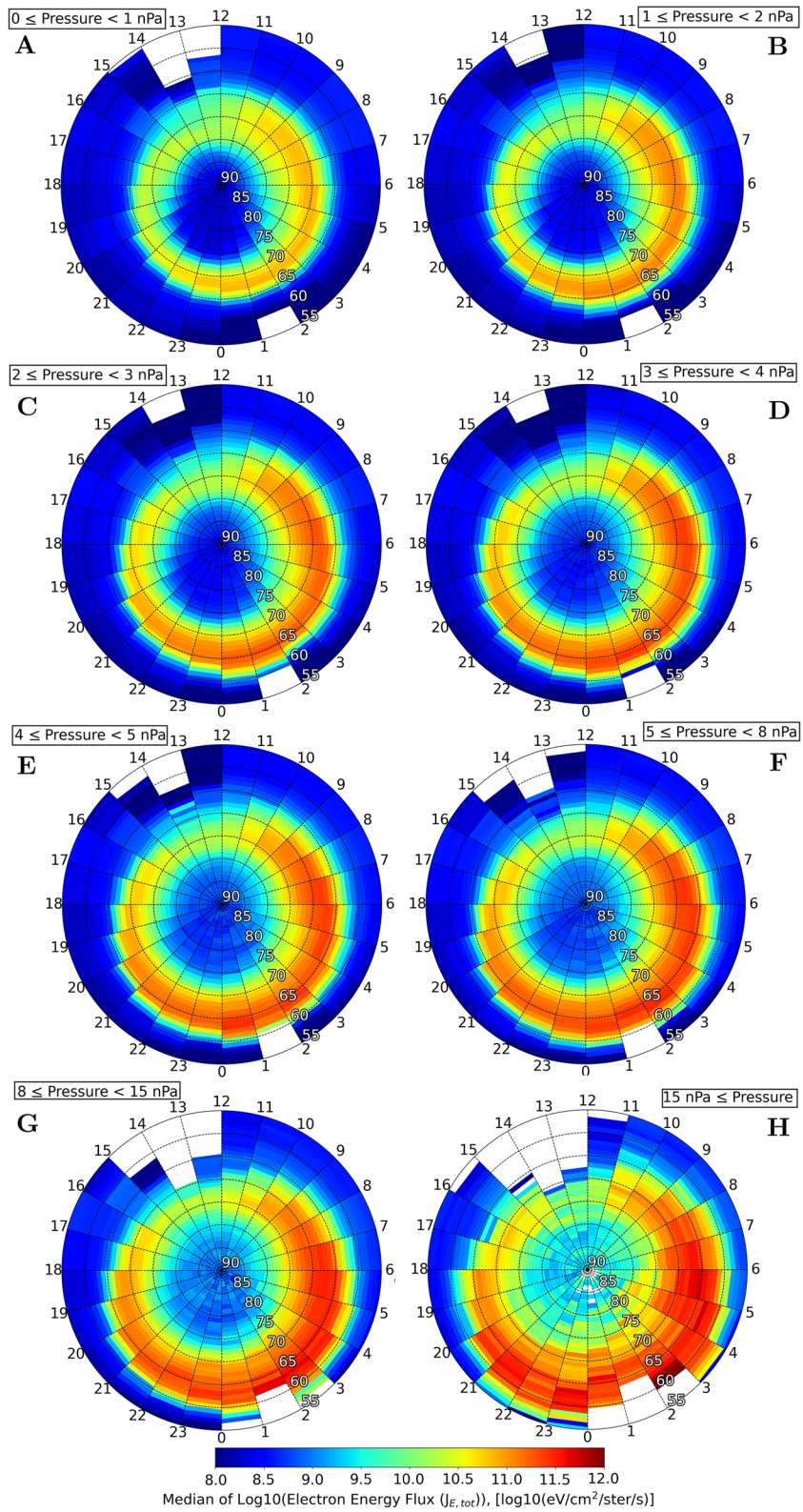

Figure 3. Median of Log_{10} ($J_{E,\mathrm{tot}}$) [eV/cm^2/ster/s] for solar wind pressure respectively between 0 and 1 nPa (a), 1 and 2 nPa (b), 2 and 3 nPa (c), 3 and 4 nPa (d), 4 and 5 nPa (e), 5 and 8 nPa (f), 8 and 15 nPa (g), 15 nPa and infinity (h).

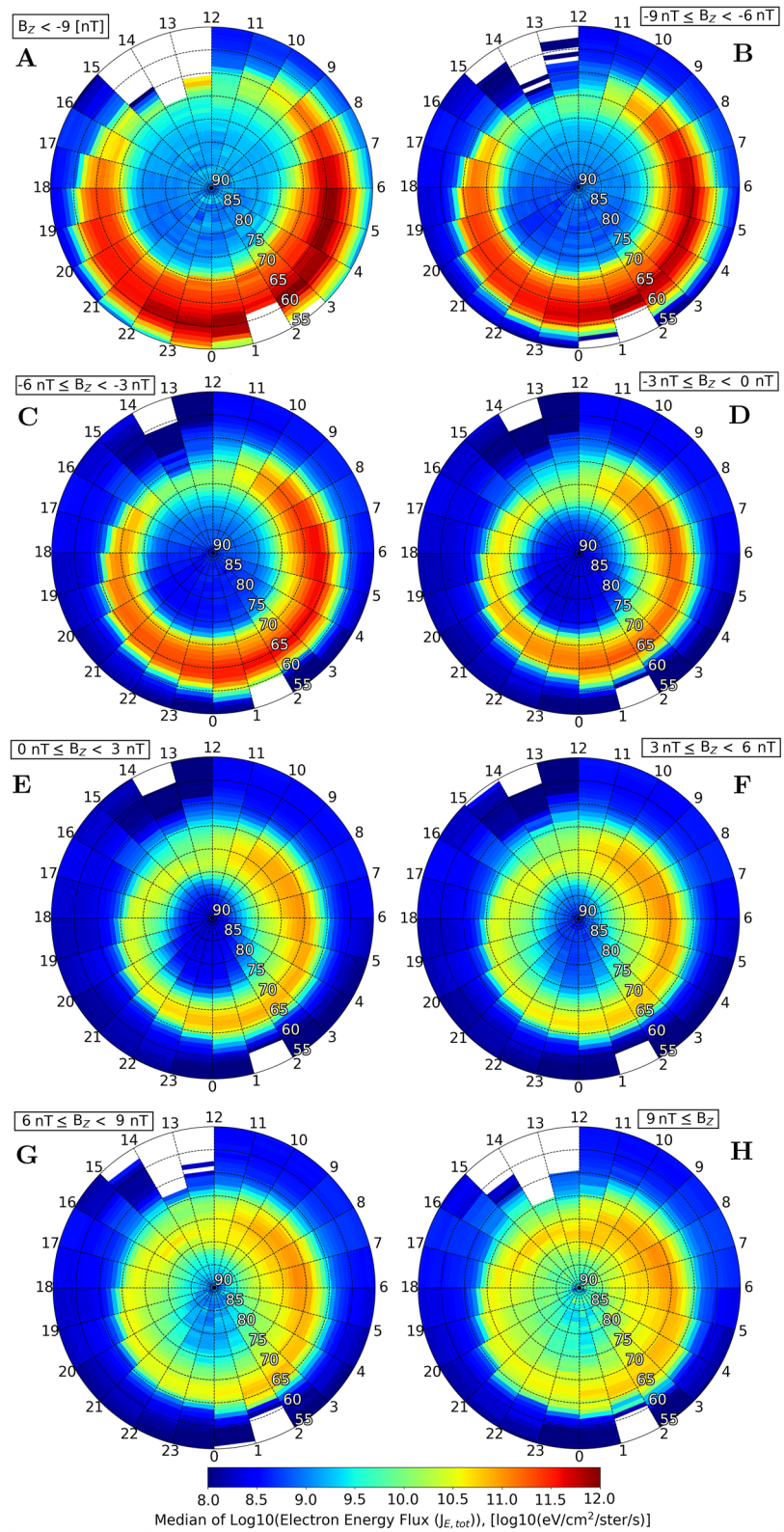

Figure 4. Median of Log_{10} ($J_{E,\mathrm{tot}}$) [eV/cm^2/ster/s] for B_z GSM respectively below −9 nT (a), between −9 and −6 nT (b), −6 and −3 nT (c), −3 and 0 nT (d), 0 and 3 nT (e), 3 and 6 nT (f), 6 and 9 nT (g), and above 9 nT (h).

- As the solar wind density increases, the behavior of the auroral oval width becomes more complex, with variations observed in different regions at different times.

As a consequence of increasing the solar wind dynamic pressure at the BSN:

- Electron energy flux increases almost monotonically, as expected by the correlation between velocity and pressure.
- Auroral oval width increases and extends equatorward.
- Polar rain increases as the dynamic pressure enhances. The increase is even clearer than that for solar wind velocity and density.

Concerning the IMF Z-component:

- As the southward component of the IMF B_z increases, the magnetosphere can become more active due to substorms or storms, resulting in particle injections and energization of the particle population in the magnetotail. The peak value of electron energy flux gradually shifts to the interval between 05:00 and 10:00 MLT as the southward component of the IMF B_z increases from negative to positive values. Overall energy flux increases with $|B_z|$ but large negative B_z means more intense oval than for large positive values.
- A clear dependence can be observed with the shapes of both the oval and the polar cap. A large southward component of the IMF generally causes the boundary to move equatorward, while a northward component moves the boundary poleward. The oval width as a function B_z seems to have a "U" shape.
- The polar cap activity as a function B_z has a "V" shape.
- The polar rain energy fluxes increase when $|B_z|$ increases.

These results can be useful for comparisons to electron precipitation models (Newell et al., 2014, 2002; Wiltberger et al., 2009; Zhu et al., 2021) and to electron precipitation reconstructions based on ionospheric simulations (Simon Wedlund et al., 2013). As a follow-up study, we will examine the effects of IMF B_y and B_x on the auroral oval and polar cap (polar rain) electron precipitation, and we will investigate the dependence of solar wind clock angle (arctan(IMF-B_y/IMF-B_z)), cone angle (arctan(IMF-B_z/IMF-B_x)), and azimuthal angle (arctan(IMF-B_y/IMF-B_x)) on the polar cap electron flux enhancements.

Appendix A: Additional Figures

Figures A1–A4 presented in this appendix show line plots of three subfigures for each solar wind parameter considered. These subfigures depict the median of the total electron flux inside the auroral oval, the median of the total electron flux inside the polar cap, and the approximate width of the auroral oval. It is important to note that we defined the boundary of the auroral oval arbitrarily as 10 log10 (eV/cm^2/s/ster). In each of the line plots shown in the four figures presented in this appendix, the *x*-axis represents the median value of either the total electron flux inside the auroral oval or the approximate width of the auroral oval, depending on the subfigure. The *y*-axis represents the median value of the solar wind parameter considered in the bin considered, as described in the main text of the paper. Thus, each point on the line plots represents a specific combination of the solar wind parameter and the electron flux. By including these additional figures in the appendix, we aim to provide a more comprehensive understanding of the complex interactions between the solar wind parameters and the Earth's

magnetosphere. We hope these figures provide a clear and more detailed visualization of the relationship between the polar zone activity, the DMSP electron flux in LEO, and the solar wind parameters.

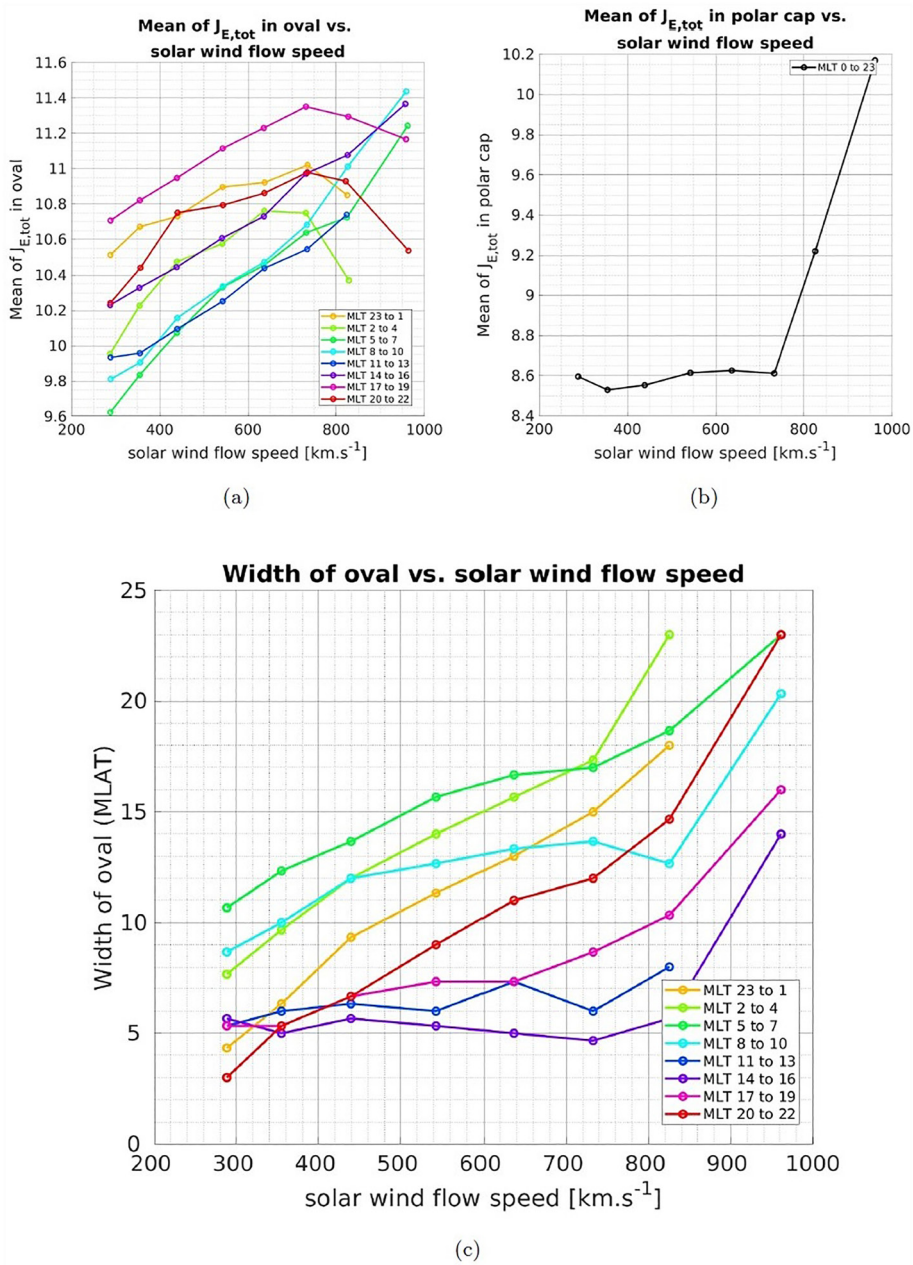

Figure A1. These line plots depict three measures as a function of solar wind flow speed. Panel (a) shows the mean of all values observed in the polar plots, where MLTs were grouped in sets of three. Each point in the polar plot corresponds to the median total electron energy flux for a specific MLAT-MLT pair. Panel (b) displays the same average, but only for values located within the auroral oval. The auroral oval is defined as the region where values exceed 10 log10 (eV/cm^2/s/ster). Finally, panel (c) shows the approximate width of the auroral oval in terms of the number of MLAT.

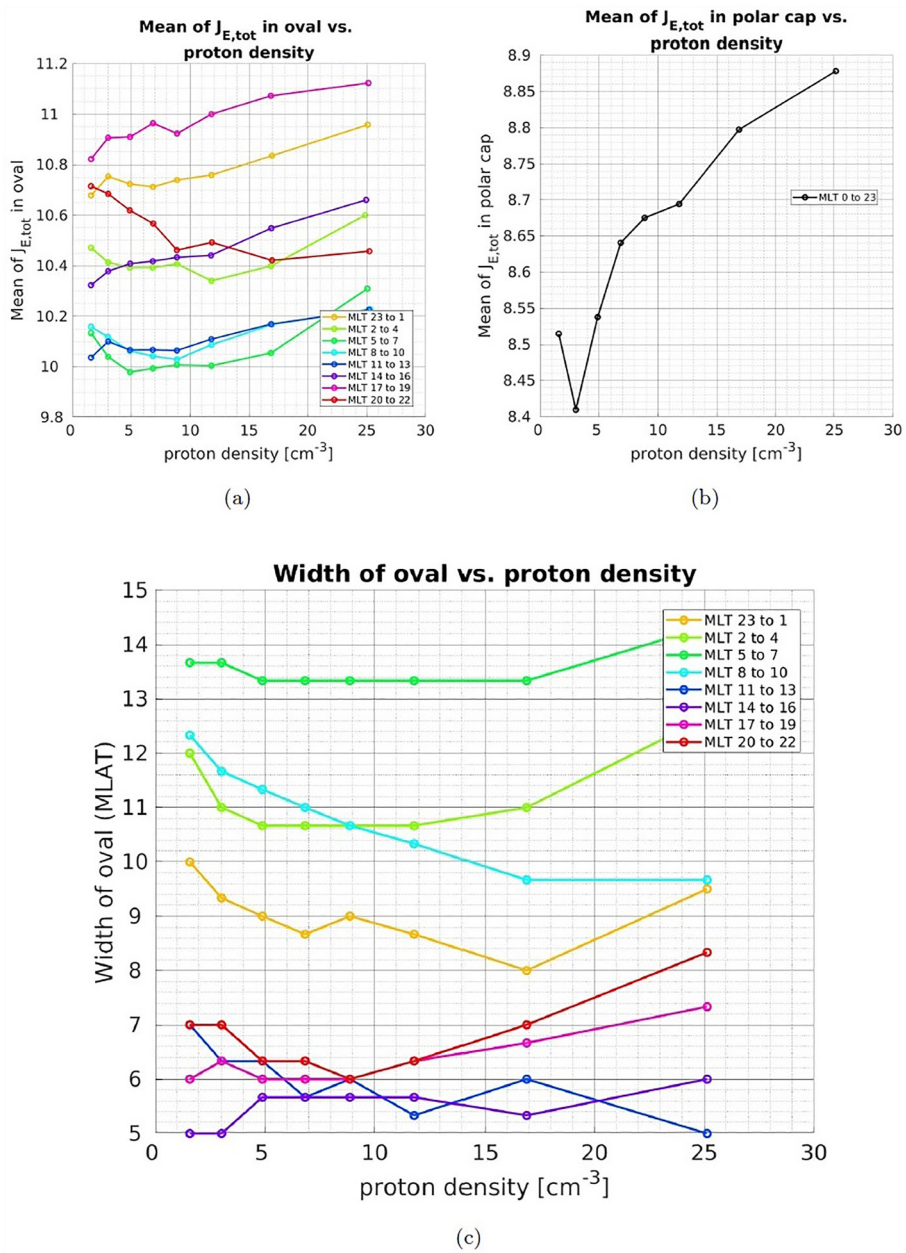

Figure A2. These line plots depict three measures as a function of solar wind proton density. Panel (a) shows the mean of all values observed in the polar plots, where MLTs were grouped in sets of three. Each point in the polar plot corresponds to the median total electron energy flux for a specific MLAT-MLT pair. Panel (b) displays the same average, but only for values located within the auroral oval. The auroral oval is defined as the region where values exceed 10 log10 (eV/cm^2/s/ster). Finally, panel (c) shows the approximate width of the auroral oval in terms of the number of MLAT.

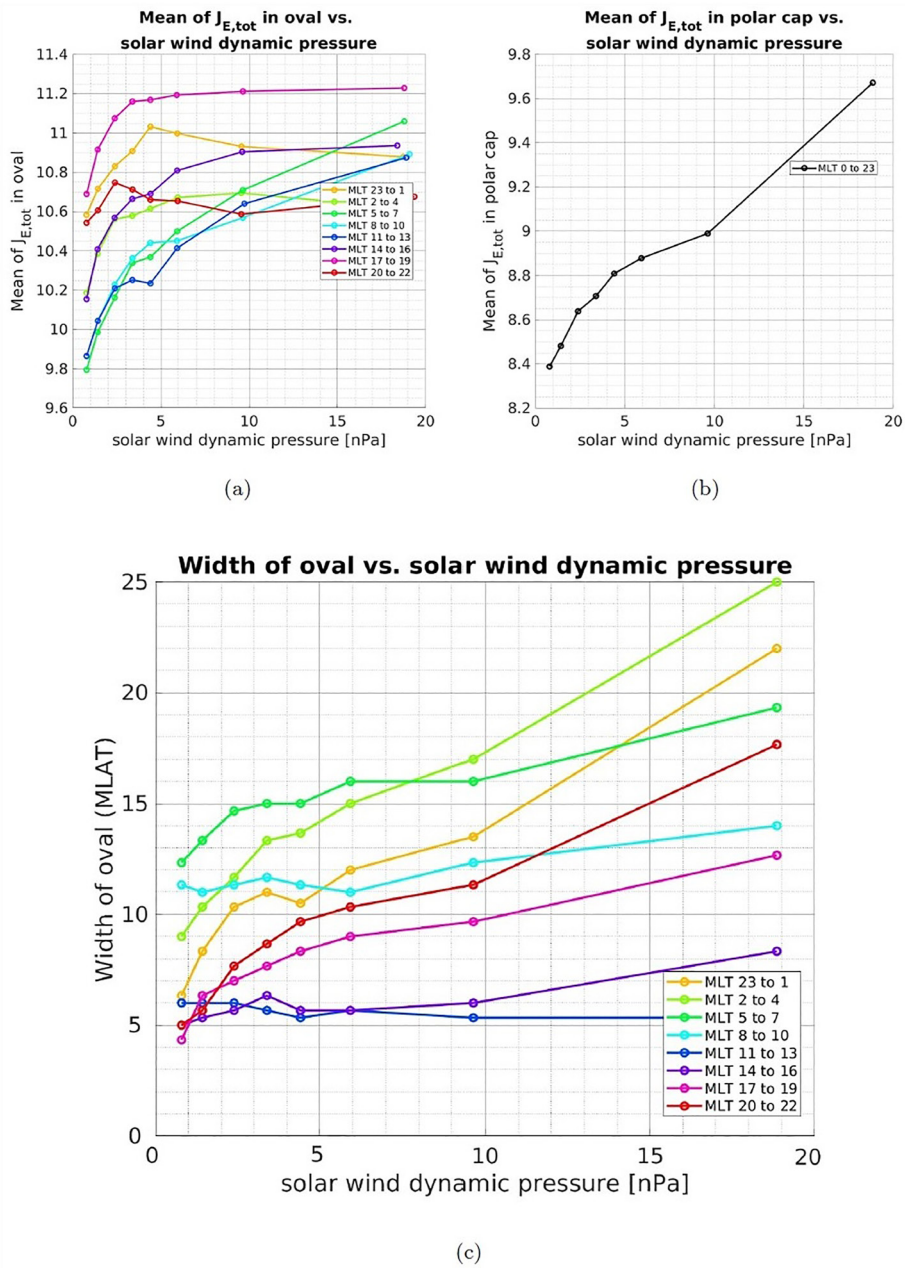

Figure A3. These line plots depict three measures as a function of solar wind dynamic pressure. Panel (a) shows the mean of all values observed in the polar plots, where MLTs were grouped in sets of three. Each point in the polar plot corresponds to the median total electron energy flux for a specific MLAT-MLT pair. Panel (b) displays the same average, but only for values located within the auroral oval. The auroral oval is defined as the region where values exceed 10 log10 (eV/cm^2/s/ster). Finally, panel (c) shows the approximate width of the auroral oval in terms of the number of MLAT.

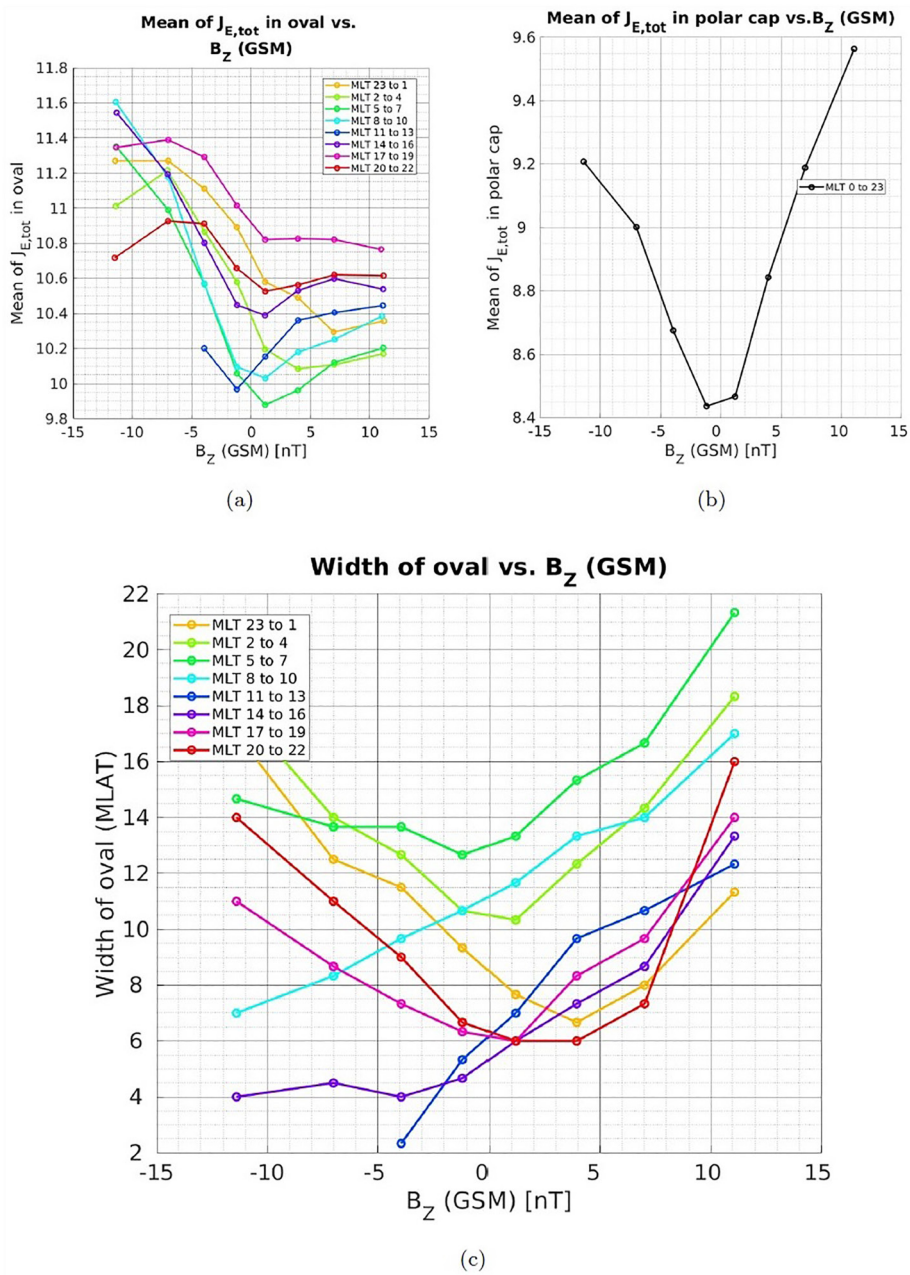

Figure A4. These line plots depict three measures as a function of IMF B_z (in GSM coordinates). Panel (a) shows the mean of all values observed in the polar plots, where MLTs were grouped in sets of three. Each point in the polar plot corresponds to the median total electron energy flux for a specific MLAT-MLT pair. Panel (b) displays the same average, but only for values located within the auroral oval. The auroral oval is defined as the region where values exceed 10 log10 (eV/cm^2/s/ster). Finally, panel (c) shows the approximate width of the auroral oval in terms of the number of MLAT.

The last four figures are representations of the magnetic latitude/magnetic longitude grid for each of the four solar wind parameters studied in the article. However, unlike the figures in the main body of the article, these figures show the density of data available for each point on the grid. Specifically, each point on the grid is color-coded according to the number of data points available for that particular combination of magnetic latitude, magnetic longitude, and solar wind parameter. These figures can help identify any gaps or biases in the data set, which can inform future research and data collection efforts. Overall, these figures are an important complement to the main

body of the article, providing additional information about the data used in the study and helping to ensure the validity and accuracy of the research findings (Figures A5–A8).

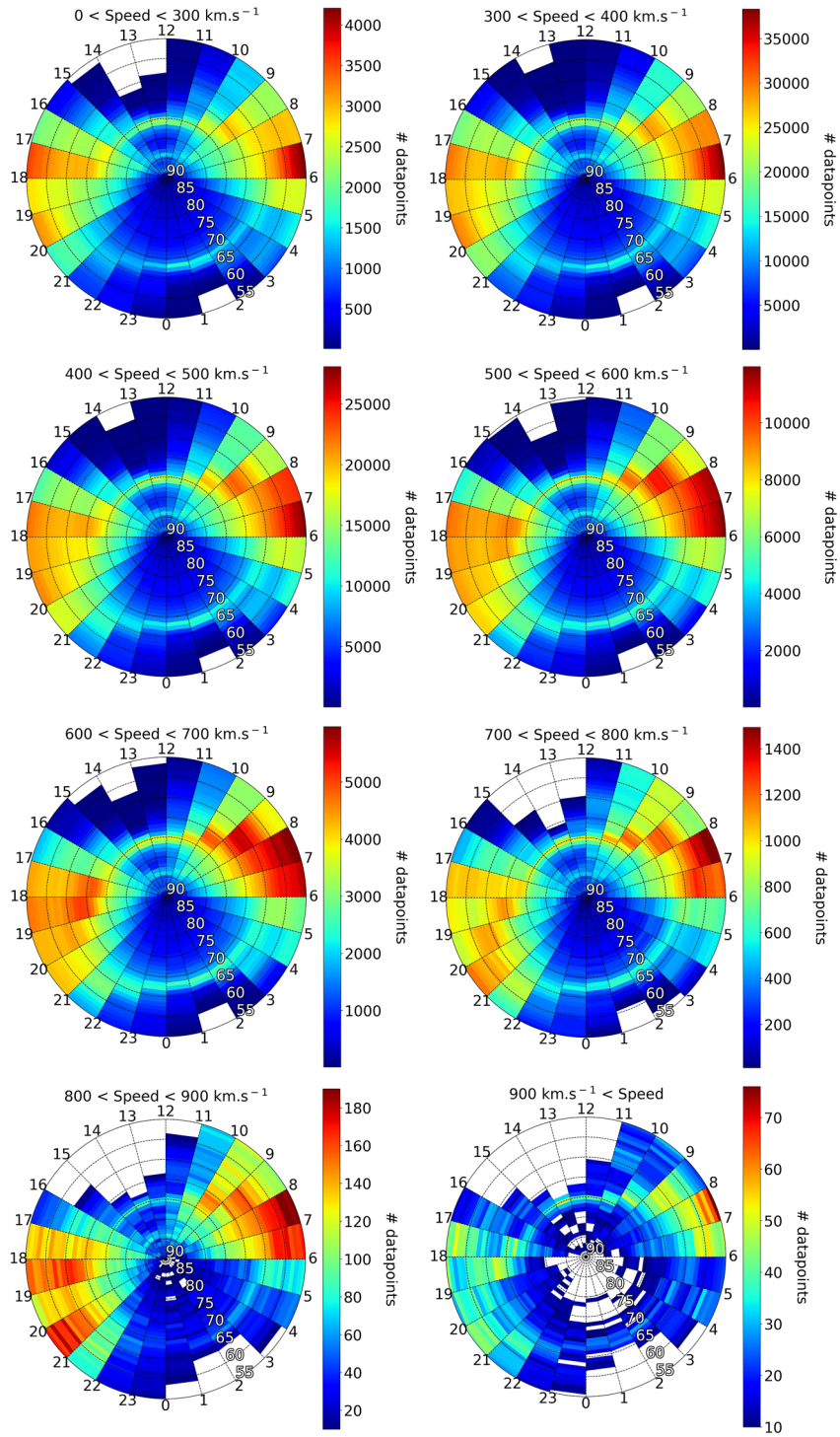

Figure A5. Number of data points available for solar wind speed (km·s^{-1}) in the same ranges than for the polar plots.

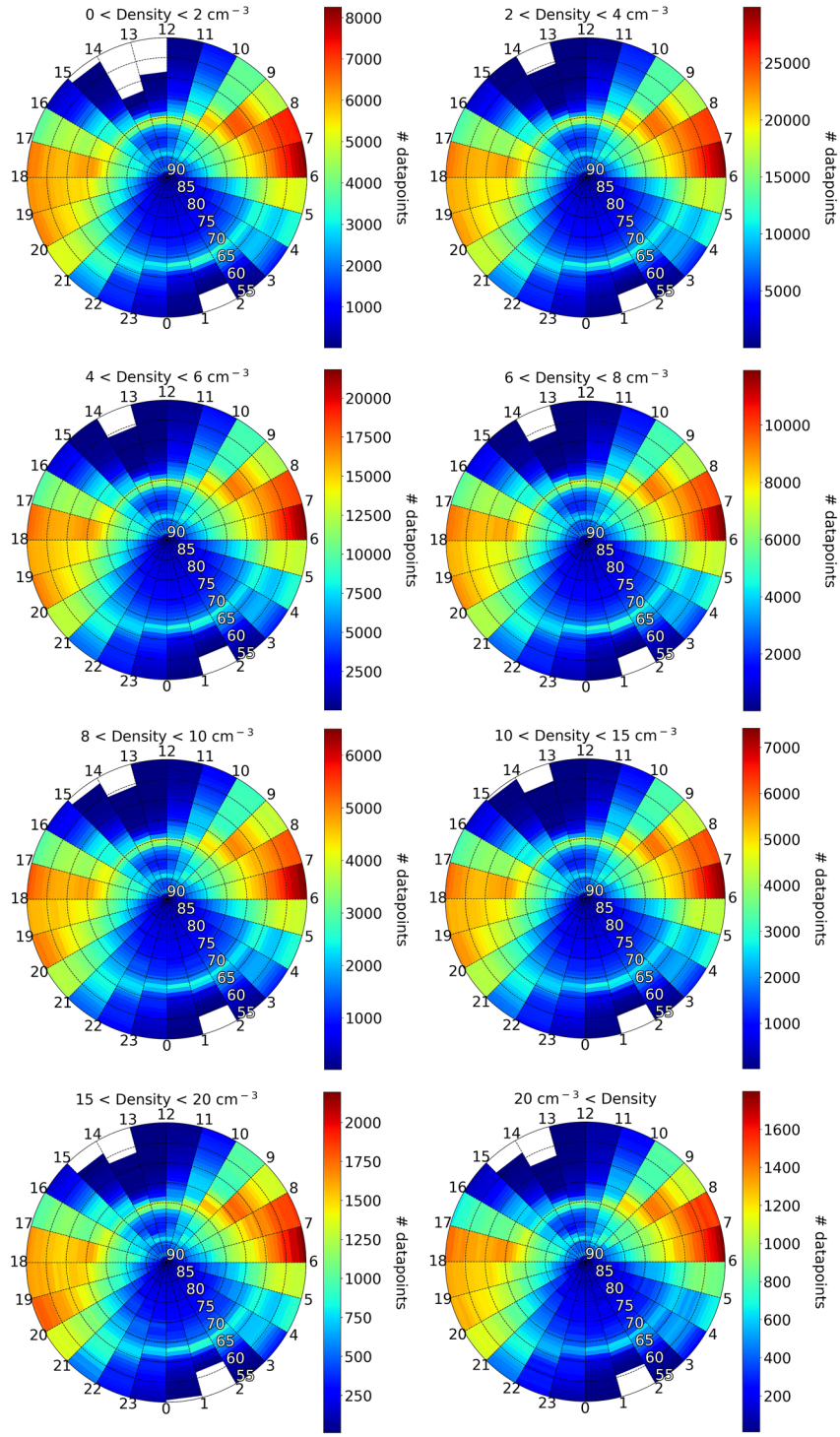

Figure A6. Number of data points available for proton density (cm^{-3}) in the same ranges than for the polar plots.

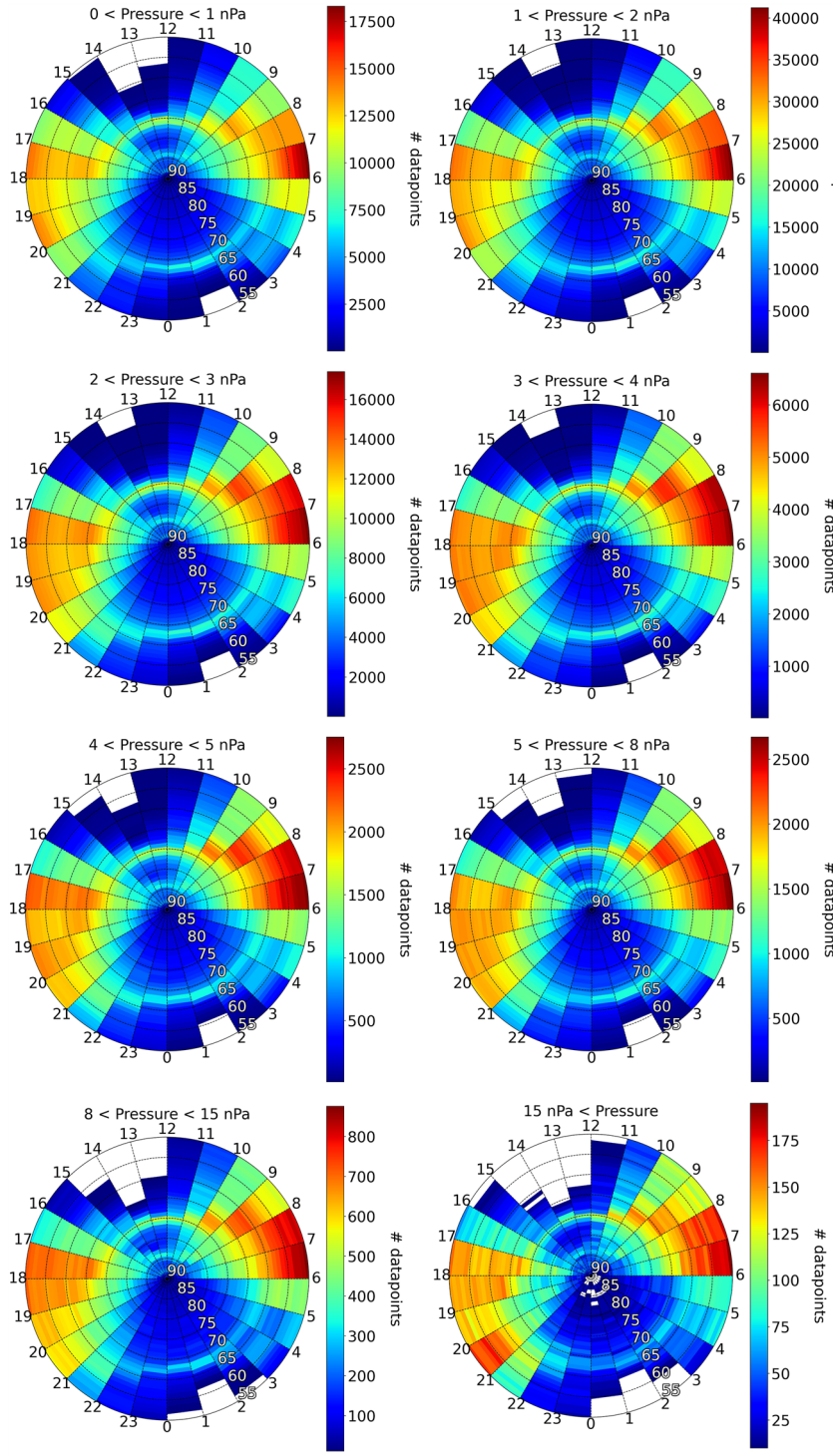

Figure A7. Number of data points available for dynamic pressure (nPa) in the same ranges than for the polar plots.

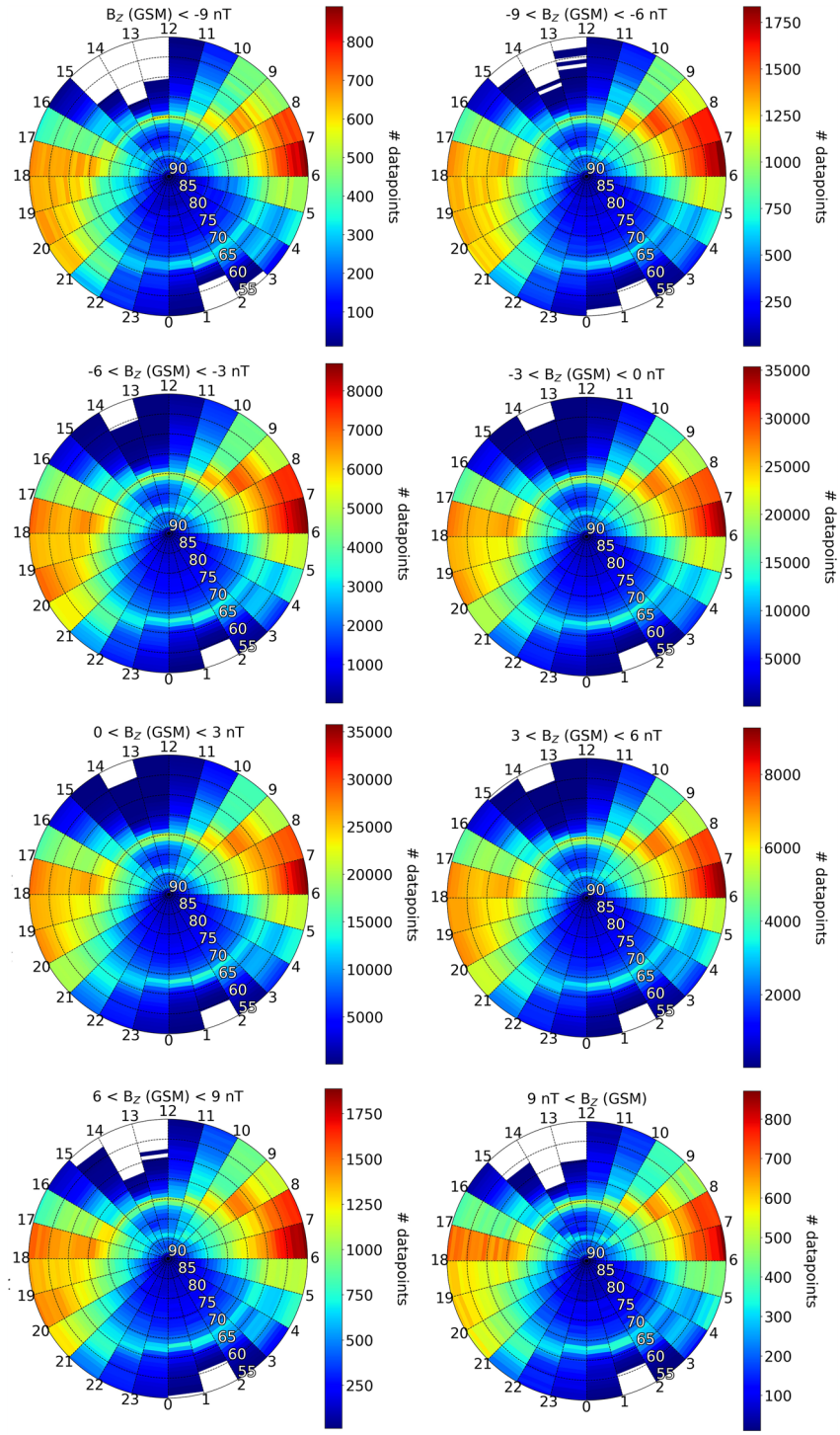

Figure A8. Number of data points available for B_z-component IMF (nT) in the same ranges than for the polar plots.

Data Availability Statement

The 1 min resolution solar wind data are available at the OMNIWeb https://omniweb.gsfc.nasa.gov/. The DMSP data are available at CDAWeb https://cdaweb.gsfc.nasa.gov/.

Acknowledgments
The authors would like to acknowledge SpaceAble and the experts who helped understand, prepare, and manage the data. The authors would like to acknowledge the NASA's CDAWeb interface and OMNIWeb database experts for providing quality and ready-to-use data. Simon Wing acknowledges the support of NASA Grants 80NSSC20K0704, 80NSSC21K1678, 80NSSC22K0515, 80NSSC21K1321, 80NSSC22K0304, 80NSSC19K0843, and 80NSSC20K0188.

References

Baker, K. B., & Wing, S. (1989). A new magnetic coordinate system for conjugate studies at high latitudes. *Journal of Geophysical Research: Space Physics*, *94*(A7), 9139–9143. https://doi.org/10.1029/JA094iA07p09139

Berchem, J., Richard, R., Escoubet, P., Wing, S., & Pitout, F. (2014). Dawn-dusk asymmetry in solar wind ion entry and dayside precipitation: Results from large-scale simulations. *Journal of Geophysical Research: Space Physics*, *119*(3), 1549–1562. https://doi.org/10.1002/2013JA019427

Berchem, J., Richard, R. L., Escoubet, C. P., Wing, S., & Pitout, F. (2016). Asymmetrical response of dayside ion precipitation to a large rotation of the IMF. *Journal of Geophysical Research: Space Physics*, *121*(1), 263–273. https://doi.org/10.1002/2015JA021969

Borovsky, J. E. (2020). What magnetospheric and ionospheric researchers should know about the solar wind. *Journal of Atmospheric and Solar-Terrestrial Physics*, *204*, 105271. https://doi.org/10.1016/j.jastp.2020.105271

Borovsky, J. E. (2021). Exploring the properties of the electron strahl at 1 AU as an indicator of the quality of the magnetic connection between the Earth and the Sun. *Frontiers in Astronomy and Space Sciences*, *8*. https://doi.org/10.3389/fspas.2021.646443

Borovsky, J. E., Thomsen, M. F., & Elphic, R. C. (1998). The driving of the plasma sheet by the solar wind. *Journal of Geophysical Research: Space Physics*, *103*(A8), 17617–17639. https://doi.org/10.1029/97JA02986

Burch, J. (1979). Effects of the interplanetary magnetic field on the auroral oval and plasmapause. *Space Science Reviews*, *23*(3), 449–464. https://doi.org/10.1007/BF00172250

Fairfield, D. H., & Scudder, J. D. (1985). Polar rain: Solar coronal electrons in the earth's magnetosphere. *Journal of Geophysical Research: Space Physics*, *90*(A5), 4055–4068. https://doi.org/10.1029/JA090iA05p04055

Fairfield, D. H., Wing, S., Newell, P. T., Ruohoniemi, J. M., Gosling, J. T., & Skoug, R. M. (2008). Polar rain gradients and field-aligned polar cap potentials. *Journal of Geophysical Research: Space Physics*, *113*(A10). https://doi.org/10.1029/2008JA013437

Feldstein, Y. I. (2016). The discovery and the first studies of the auroral oval: A review. *Geomagnetism and Aeronomy*, *56*(2), 129–142. https://doi.org/10.1134/S0016793216020043

Fujimoto, M., Terasawa, T., Mukai, T., Saito, Y., Yamamoto, T., & Kokubun, S. (1998). Plasma entry from the flanks of the near-earth magnetotail: Geotail observations. *Journal of Geophysical Research: Space Physics*, *103*(A3), 4391–4408. https://doi.org/10.1029/97JA03340

Gabrielse, C., Nishimura, T., Chen, M., Hecht, J. H., Kaeppler, S. R., Gillies, D. M., et al. (2021). Estimating precipitating energy flux, average energy, and hall auroral conductance from THEMIS all-sky-imagers with focus on mesoscales. *Frontiers in Physics*, *9*. https://doi.org/10.3389/fphy.2021.744298

Gussenhoven, M. S., Hardy, D. A., Heinemann, N., & Burkhardt, R. K. (1984). Morphology of the polar rain. *Journal of Geophysical Research: Space Physics*, *89*(A11), 9785–9800. https://doi.org/10.1029/JA089iA11p09785

Hardy, D., Schmitt, L., Gussenhoven, M., Marshall, F., & Yeh, H. (1984). Precipitating electron and ion detectors (SSJ/4) for the block 5D/flights 6–10 DMSP (defense meteorological satellite program) satellites: Calibration and data presentation. Rep. AFGL-TR-84-0317.

Johnson, J. R., Wing, S., Delamere, P., Petrinec, S., & Kavosi, S. (2021). Field-aligned currents in auroral vortices. *Journal of Geophysical Research: Space Physics*, *126*(2), e2020JA028583. https://doi.org/10.1029/2020JA028583

Kamide, Y., Perreault, P. D., Akasofu, S. I., & Winningham, J. D. (1977). Dependence of substorm occurrence probability on the interplanetary magnetic field and on the size of the auroral oval. *Journal of Geophysical Research*, *82*(35), 5521–5528. https://doi.org/10.1029/JA082i035p05521

King, J., & Papitashvili, N. (2006). *One min and 5-min solar wind data sets at the Earth's bow shock nose*. NASA Goddard Space Flight Center.

Liou, K., Newell, P. T., Shue, J.-H., Meng, C.-I., Miyashita, Y., Kojima, H., & Matsumoto, H. (2007). "Compression aurora": Particle precipitation driven by long-duration high solar wind ram pressure. *Journal of Geophysical Research: Space Physics*, *112*(A11). https://doi.org/10.1029/2007JA012443

Lockwood, M., Denig, W. F., Farmer, A. D., Davda, V. N., Cowley, S. W. H., & Lühr, H. (1993). Ionospheric signatures of pulsed reconnection at the Earth's magnetopause. *Nature*, *361*(6411), 424–428. https://doi.org/10.1038/361424a0

Lyons, L. R., Schulz, M., Pridmore-Brown, D. C., & Roeder, J. L. (1994). Low-latitude boundary layer near noon: An open field line model. *Journal of Geophysical Research: Space Physics*, *99*(A9), 17367–17377. https://doi.org/10.1029/94JA00867

Maggiolo, R., Hamrin, M., De Keyser, J., Pitkänen, T., Cessateur, G., Gunell, H., & Maes, L. (2017). The delayed time response of geomagnetic activity to the solar wind. *Journal of Geophysical Research: Space Physics*, *122*(11), 11109–11127. https://doi.org/10.1002/2016JA023793

Milan, S. E., Cowley, S. W. H., Lester, M., Wright, D. M., Slavin, J. A., Fillingim, M., & Singer, H. J. (2004). Response of the magnetotail to changes in the open flux content of the magnetosphere. *Journal of Geophysical Research: Space Physics*, *109*(A4). A04220. https://doi.org/10.1029/2003ja010350

Newell, P. T., Liou, K., Gjerloev, J., Sotirelis, T., Wing, S., & Mitchell, E. (2016). Substorm probabilities are best predicted from solar wind speed. *Journal of Atmospheric and Solar-Terrestrial Physics*, *146*, 28–37. https://doi.org/10.1016/j.jastp.2016.04.019

Newell, P. T., Liou, K., & Wilson, G. R. (2009). Polar cap particle precipitation and aurora: Review and commentary. *Journal of Atmospheric and Solar-Terrestrial Physics*, *71*(2), 199–215. https://doi.org/10.1016/j.jastp.2008.11.004

Newell, P. T., Liou, K., Zhang, Y., Sotirelis, T., Paxton, L. J., & Mitchell, E. J. (2014). Ovation Prime-2013: Extension of auroral precipitation model to higher disturbance levels. *Space Weather*, *12*(6), 368–379. https://doi.org/10.1002/2014SW001056

Newell, P. T., & Meng, C.-I. (1992). Mapping the dayside ionosphere to the magnetosphere according to particle precipitation characteristics. *Geophysical Research Letters*, *19*(6), 609–612. https://doi.org/10.1029/92GL00404

Newell, P. T., Ruohoniemi, J. M., & Meng, C.-I. (2004). Maps of precipitation by source region, binned by IMF, with inertial convection streamlines. *Journal of Geophysical Research: Space Physics*, *109*(A10), A10206. https://doi.org/10.1029/2004JA010499

Newell, P. T., Sotirelis, T., Ruohoniemi, J. M., Carbary, J. F., Liou, K., Skura, J. P., et al. (2002). Ovation: Oval variation, assessment, tracking, intensity, and online nowcasting. *Annales Geophysicae*, *20*(7), 1039–1047. https://doi.org/10.5194/angeo-20-1039-2002

Newell, P. T., Sotirelis, T., & Wing, S. (2009). Diffuse, monoenergetic, and broadband aurora: The global precipitation budget. *Journal of Geophysical Research: Space Physics*, *114*(A9). https://doi.org/10.1029/2009JA014326

Newell, P. T., Sotirelis, T., & Wing, S. (2010). Seasonal variations in diffuse, monoenergetic, and broadband aurora. *Journal of Geophysical Research: Space Physics*, *115*(A3). https://doi.org/10.1029/2009JA014805

Newell, P. T., Wing, S., Meng, C.-I., & Sigillito, V. (1991). The auroral oval position, structure, and intensity of precipitation from 1984 onward: An automated on-line data base. *Journal of Geophysical Research: Space Physics*, *96*(A4), 5877–5882. https://doi.org/10.1029/90JA02450

Newell, P. T., Xu, D., Meng, C.-I., & Kivelson, M. G. (1997). Dynamical polar cap: A unifying approach. *Journal of Geophysical Research: Space Physics*, *102*(A1), 127–139. https://doi.org/10.1029/96JA03045

Ni, B., Thorne, R. M., Zhang, X., Bortnik, J., Pu, Z., Xie, L., et al. (2016). Origins of the Earth's diffuse auroral precipitation. *Space Science Reviews*, *200*(1), 205–259. https://doi.org/10.1007/s11214-016-0234-7

Reeves, G. D., Chan, A., & Rodger, C. (2009). New directions for radiation belt research. *Space Weather*, *7*(7). https://doi.org/10.1029/2008SW000436

Riehl, K. B., & Hardy, D. A. (1986). Average characteristics of the polar rain and their relationship to the solar wind and the interplanetary magnetic field. *Journal of Geophysical Research: Space Physics*, *91*(A2), 1557–1571. https://doi.org/10.1029/JA091iA02p01557

Sergeev, V. A., Liou, K., Newell, P. T., Ohtani, S.-I., Hairston, M. R., & Rich, F. (2004). Auroral streamers: Characteristics of associated precipitation, convection and field-aligned currents. *Annales Geophysicae*, *22*(2), 537–548. https://doi.org/10.5194/angeo-22-537-2004

Shi, Q. Q., Zong, Q.-G., Fu, S., Dunlop, M., Pu, Z., Parks, G., et al. (2013). Solar wind entry into the high-latitude terrestrial magnetosphere during geomagnetically quiet times. *Nature Communications*, *4*(1), 1466. https://doi.org/10.1038/ncomms2476

Shi, Q. Q., Zong, Q.-G., Zhang, H., Pu, Z. Y., Fu, S. Y., Xie, L., et al. (2009). Cluster observations of the entry layer equatorward of the cusp under northward interplanetary magnetic field. *Journal of Geophysical Research: Space Physics*, *114*(A12). https://doi.org/10.1029/2009JA014475

Simon Wedlund, C., Lamy, H., Gustavsson, B., Sergienko, T., & Brändström, U. (2013). Estimating energy spectra of electron precipitation above auroral arcs from ground-based observations with radar and optics. *Journal of Geophysical Research: Space Physics*, *118*(6), 3672–3691. https://doi.org/10.1002/jgra.50347

Sorathia, K. A., Merkin, V. G., Ukhorskiy, A. Y., Allen, R. C., Nykyri, K., & Wing, S. (2019). Solar wind ion entry into the magnetosphere during northward IMF. *Journal of Geophysical Research: Space Physics*, *124*(7), 5461–5481. https://doi.org/10.1029/2019JA026728

Summers, D., Thorne, R. M., & Xiao, F. (1998). Relativistic theory of wave-particle resonant diffusion with application to electron acceleration in the magnetosphere. *Journal of Geophysical Research: Space Physics*, *103*(A9), 20487–20500. https://doi.org/10.1029/98JA01740

Thorne, R. M. (2010). Radiation belt dynamics: The importance of wave-particle interactions. *Geophysical Research Letters*, *37*(22). https://doi.org/10.1029/2010gl044990

Troshichev, O., Gusev, M., Nickolashkin, S., & Samsonov, V. (1988). Features of the polar cap aurorae in the southern polar region. *Planetary and Space Science*, *36*(5), 429–439. https://doi.org/10.1016/0032-0633(88)90102-X

Tulegenov, B., Raeder, J., Cramer, W. D., Ferdousi, B., Fuller-Rowell, T. J., Maruyama, N., & Strangeway, R. J. (2023). Storm time polar cap expansion: Interplanetary magnetic field clock angle dependence. *Annales Geophysicae*, *41*(1), 39–54. https://doi.org/10.5194/angeo-41-39-2023

Wiltberger, M., Weigel, R. S., Lotko, W., & Fedder, J. A. (2009). Modeling seasonal variations of auroral particle precipitation in a global-scale magnetosphere-ionosphere simulation. *Journal of Geophysical Research: Space Physics*, *114*(A1). https://doi.org/10.1029/2008JA013108

Wing, S., Berchem, J., Escoubet, C. P., Farrugia, C., & Lugaz, N. (2023). Multispacecraft observations of the simultaneous occurrence of magnetic reconnection at high and low latitudes during the passage of a solar wind rotational discontinuity embedded in the April 9–11, 2015 ICME. *Geophysical Research Letters*, *50*(9), e2023GL103194. https://doi.org/10.1029/2023GL103194

Wing, S., Fairfield, D. H., Johnson, J. R., & Ohtani, S.-I. (2015). On the field-aligned electric field in the polar cap. *Geophysical Research Letters*, *42*(13), 5090–5099. https://doi.org/10.1002/2015GL064229

Wing, S., Gkioulidou, M., Johnson, J. R., Newell, P. T., & Wang, C.-P. (2013). Auroral particle precipitation characterized by the substorm cycle. *Journal of Geophysical Research: Space Physics*, *118*(3), 1022–1039. https://doi.org/10.1002/jgra.50160

Wing, S., & Johnson, J. R. (2009). Substorm entropies. *Journal of Geophysical Research Space Physics*, *114*(A9). https://doi.org/10.1029/2008JA013989

Wing, S., Johnson, J. R., Camporeale, E., & Reeves, G. D. (2016). Information theoretical approach to discovering solar wind drivers of the outer radiation belt. *Journal of Geophysical Research: Space Physics*, *121*(10), 9378–9399. https://doi.org/10.1002/2016JA022711

Wing, S., Johnson, J. R., Chaston, C. C., Echim, M., Escoubet, C. P., Lavraud, B., et al. (2014). Review of solar wind entry into and transport within the plasma sheet. *Space Science Reviews*, *184*(1), 33–86. https://doi.org/10.1007/s11214-014-0108-9

Wing, S., Johnson, J. R., & Fujimoto, M. (2006). Timescale for the formation of the cold-dense plasma sheet: A case study. *Geophysical Research Letters*, *33*(23), L23106. https://doi.org/10.1029/2006GL027110

Wing, S., Johnson, J. R., Newell, P. T., & Meng, C.-I. (2005). Dawn-dusk asymmetries, ion spectra, and sources in the northward interplanetary magnetic field plasma sheet. *Journal of Geophysical Research: Space Physics*, *110*(A8). https://doi.org/10.1029/2005JA011086

Wing, S., Johnson, J. R., Turner, D. L., Ukhorskiy, A. Y., & Boyd, A. J. (2022). Untangling the solar wind and magnetospheric drivers of the radiation belt electrons. *Journal of Geophysical Research: Space Physics*, *127*(4), e2021JA030246. https://doi.org/10.1029/2021JA030246

Wing, S., & Newell, P. T. (1998). Central plasma sheet ion properties as inferred from ionospheric observations. *Journal of Geophysical Research: Space Physics*, *103*(A4), 6785–6800. https://doi.org/10.1029/97JA02994

Wing, S., Newell, P. T., & Onsager, T. G. (1996). Modeling the entry of magnetosheath electrons into the dayside ionosphere. *Journal of Geophysical Research*, *101*(A6), 13155–13167. https://doi.org/10.1029/96JA00395

Wing, S., Newell, P. T., & Ruohoniemi, J. M. (2001). Double cusp: Model prediction and observational verification. *Journal of Geophysical Research: Space Physics*, *106*(A11), 25571–25593. https://doi.org/10.1029/2000JA000402

Zhu, Q., Deng, Y., Maute, A., Kilcommons, L. M., Knipp, D. J., & Hairston, M. (2021). Ashley: A new empirical model for the high-latitude electron precipitation and electric field. *Space Weather*, *19*(5), e2020SW002671. https://doi.org/10.1029/2020SW002671

Zhu, Q., Deng, Y., Richmond, A., & Maute, A. (2018). Small-scale and mesoscale variabilities in the electric field and particle precipitation and their impacts on joule heating. *Journal of Geophysical Research: Space Physics*, *123*(11), 9862–9872. https://doi.org/10.1029/2018JA025771